

# Projection method for improving signal to noise ratio of localized surface plasmon resonance biosensors

AHMED ABUMAZWED,<sup>1,\*</sup> WAKANA KUBO,<sup>2</sup> CHEN SHEN,<sup>1</sup> TAKUO TANAKA,<sup>3</sup> AND ANDREW G. KIRK<sup>1</sup>

<sup>1</sup>ECE Dept., McGill University, 3480 University Street, Montreal, H3A 2A9, Canada

<sup>2</sup>Department of Electrical and Electronic Engineering, Tokyo University of Agriculture and Technology, 2-24-16 Naka-cho, Koganei-shi, Tokyo, 184-8588, Japan

<sup>3</sup>Metamaterials Lab., RIKEN, 2-1 Hirosawa, Wako, Saitama, 351-0198, Japan

\*Ahmed.Abumazwed@mail.mcgill.ca

**Abstract:** This paper presents a simple and accurate method (the projection method) to improve the signal to noise ratio of localized surface plasmon resonance (LSPR). The nanostructures presented in the paper can be readily fabricated by nanoimprint lithography. The finite difference time domain method is used to simulate the structures and generate a reference matrix for the method. The results are validated against experimental data and the proposed method is compared against several other recently published signal processing techniques. We also apply the projection method to biotin-streptavidin binding experimental data and determine the limit of detection (LoD). The method improves the signal to noise ratio (SNR) by one order of magnitude, and hence decreases the limit of detection when compared to the direct measurement of the transmission-dip. The projection method outperforms the established methods in terms of accuracy and achieves the best combination of signal to noise ratio and limit of detection.

© 2016 Optical Society of America

**OCIS codes:** (120.3890) Medical optics instrumentation; (130.6010) Sensors; (170.4520) Optical confinement and manipulation; (280.1415) Biological sensing and sensors; (280.4788) Optical sensing and sensors; (240.6680) Surface plasmons; (350.4238) Nanophotonics and photonic crystals.

## References and links

1. A. J. Haes, R. P. Van Duyne, "A nanoscale optical biosensor: sensitivity and selectivity of an approach based on the localized surface plasmon resonance spectroscopy of triangular silver nanoparticles," *J. Am. Chem. Soc.*, **124**(35), 10596–10604 (2002).
2. J. Cao, T. Suna and K. T.V. Grattana, "Gold nanorod-based localized surface plasmon resonance biosensors: A review," *Sensors and Actuators B: Chemical*, **195**, 332–351 (2014).
3. N. Nehru, Y. Linliang, W. Yinan, and J. T. Hastings, "Using U-Shaped Localized Surface Plasmon Resonance Sensors to Compensate for Nonspecific Interactions," *IEEE Trans. Nanotechnology*, **13**(1), 55–61 (2014).
4. A. F. Coskun, A. E. Cetin, B. C. Galarreta, D. A. Alvarez, H. Altug, and A. Ozcan, "Lensfree optofluidic plasmonic sensor for real-time and label-free monitoring of molecular binding events over a wide field-of-view," *Sci. Rep.*, **4**, 6789 (2014).
5. W. Kubo and S. Fujikawa, "Au Double Nanopillars with Nanogap for Plasmonic Sensor," *Nano Letters* **11**(1), 8–15 (2011).
6. S. J. Zalyubovskiy, M. Bogdanova, A. Deinega, Y. Lozovik, A. D. Pris, K. H. An, W. P. Hall, and R. A. Potyrailo, "Theoretical limit of localized surface plasmon resonance sensitivity to local refractive index change and its comparison to conventional surface plasmon resonance sensor," *J. Opt. Soc. Am. A* **29**(6), 994–1002 (2012).
7. K. Johansen, R. Stalberg, I. Lundstrom, and B. Liedberg, "Surface plasmon resonance: instrumental resolution using photodiode arrays," *Meas. Sci. Technol.* **11**(11), 1630–1638 (2000).
8. R. E. Messersmith, G. J. Nusz, and S. M. Reed, "Using the Localized Surface Plasmon Resonance of Gold Nanoparticles to Monitor Lipid Membrane Assembly and Protein Binding," *J. Phys. Chem. C Nanomater Interfaces* **117**(50), 26725–26733 (2013).
9. G. G. Nenninger, M. Piliarik and J. Homola, "Data analysis for optical sensors based on spectroscopy of surface plasmons," *Meas. Sci. Technol.*, **13**, 2038 (2002).
10. K. S. Johnston, K. S. Booksh, T. M. Chinowsky, and S. S. Yee, "Performance comparison between high and low resolution spectrophotometers used in a white light surface plasmon resonance sensor," *Sens. Actuators B, Chem.*, **54**(1/2), 80–88 (1999).

11. T. M. Chinowsky, L. S. Jung, and S. S. Yee, "Optimal linear data analysis for surface plasmon resonance biosensors," *Sens. Actuators B, Chem.*, **54**(1/2), 89–97 (1999).
12. E. Stenberg, B. Persson, H. Roos, and C. Urbaniczky, "Quantitative determination of surface concentration of protein with surface plasmon resonance using radiolabeled proteins," *J. Colloid Interface Sci.*, **143**(2), 513–526 (1991).
13. A. Barnett and E. M. Goldys, "Modeling of the SPR resolution enhancement for conventional and nanoparticle inclusive sensors by using statistical hypothesis testing," *Opt. Express* **18**(9), 9384–9397 (2010).
14. C. J. Alleyne, A. G. Kirk, W.-Y. Chien, and P. G. Charette, "Numerical method for high accuracy index of refraction estimation for spectro-angular surface plasmon resonance systems," *Opt. Express* **16**(24), 19493–19503 (2008).
15. M. Das, D. Hohertz, R. Nirwan, A. G. Brolo, K. L. Kavanagh, R. Gordon, "Improved Performance of Nanohole Surface Plasmon Resonance Sensors by the Integrated Response Method," *Photonics Journal, IEEE* **3**(3), 441–449 (2011).
16. T. W. Ebbesen, H. J. Lezec, H. F. Ghaemi, T. Thio and P. A. Wolff, "Extraordinary optical transmission through sub-wavelength hole arrays," *Nature* **391**(6668), 667–669 (1998).
17. T. D. Visser, "Plasmonics: Surface plasmons at work?," *Nature Physics* **2**(8), 509 – 510 (2006).
18. C. Genet and T. W. Ebbesen, "Light in tiny holes," *Nature* **445**(7123), 39–46 (2007).
19. M. Schwind, B. Kasemo, and I. Zorić, "Localized and Propagating Plasmons in Metal Films with Nanoholes," *Nano Letters*, **13**(4), 1743–1750 (2013).
20. M. E. Stewart, J. Tao, J. Maria, S. K. Gray and J. A. Rogers, "Multispectral thin film biosensing and quantitative imaging using 3D plasmonic crystals," *Anal. Chem.* **81**(15), 5980–5989 (2009).
21. OptiFDTD-Designer, version 12.0.0.618, optiwave, <http://www.optiwave.com>
22. G.M. Whitesides, E. Ostuni, S. Takayama, X.Y. Jiang, and D.E. Ingber, "Soft lithography in biology and biochemistry," *Ann. Rev. Biomed. Eng.* **3**, 335 (2001).
23. D.R. Lide, 86th Handbook of Chemistry and Physics, (CRC Press, Boca Raton 2006) Chap. 8.
24. S. Kedenburg, M. Vieweg, T. Gissibl, and H. Giessen, "Linear refractive index and absorption measurements of nonlinear optical liquids in the visible and near-infrared spectral region," *Opt. Mater. Express* **2**(11), 1588–1611 (2012).
25. E. Fujiwara, R. T. Takeishi, A. Hase, E. Ono, J. S. Santos and C.K. Susuki, "Real-time optical fibre sensor for hydro-alcoholic solutions," *Meas. Sci. Technol.* **21**, 094035 (2010).
26. Nowakowska, Janina, The Refractive Indices of Ethyl Alcohol and Water Mixtures, Master's Theses (Loyola University Chicago 1939), Paper 668.
27. S. Zhan, X. Wang and Y. Liu, "Fast centroid algorithm for determining the surface plasmon resonance angle using the fixed-boundary method," *Meas. Sci. Technol.* **22**, 025201 (2011).
28. J. M. Bingham, J. N. Anker, L. E. Kreno, and R. P. Van Duyne, "Gas Sensing with High-Resolution Localized Surface Plasmon Resonance Spectroscopy," *Journal of the American Chemical Society* **132**(49), 17358–17359 (2010).
29. Y. Shen, J. Zhou, T. Liu, Y. Tao, R. Jiang, M. Liu, G. Xiao, J. Zhu, Z.-K. Zhou, X. Wang, C. Jin and J. Wang, "Plasmonic gold mushroom arrays with refractive index sensing figures of merit approaching the theoretical limit," *Nat Commun.* **4**, 2381 (2013).

## 1. Introduction

Metallic nanostructures have attracted great attention in sensing applications due to their miniaturized dimensions, design flexibility, and biocompatibility [1–5]. Their advantages as biosensors include: easy integration into other micro/nano devices (making them good candidates for Laboratory-on-chip and point of care applications), inexpensive instrumentation, and small sample requirements. The plasmonic properties of metallic nanostructures depend on their shape and size and the ambient environment. The shape and size determine the number and location of the resonance wavelengths. An increase in the refractive index of the ambient environment red-shifts the resonance wavelength identifying the target analyte if a specific surface chemistry is used. Metallic nanostructures support localized surface plasmon resonance (LSPR) as they confine light within a small region around them leading to a short local field decay length ( $\sim 20 - 40 \text{ nm}$ ). This is less than that of conventional SPR sensors ( $\sim 200 - 500 \text{ nm}$ ), making metallic nanostructures more specific to target analytes and minimizing interference due to changes in the buffer solution. However, their sensitivity and SNR are limited by the short decay length, affecting the accuracy of the results [6].

Metallic nanostructure-based sensors can operate either in wavelength or intensity interrogation modes; for the wavelength interrogation mode, the sensing chip is excited by a broadband light beam and the spectrum is collected in real time; for the intensity interrogation mode, a monochromatic laser beam excites the nanostructures, and the transmitted beam is focused

on a photodetector that measures the change in the intensity with respect to changes in bulk refractive index or surface binding events. The latter is more impacted by noise due to the intensity fluctuations of the light source, and hence the detection error is more pronounced in this case. The dip-finding method can be used to process the sensor data where the dip of the resonance curve is tracked simultaneously and a sensorgram can be generated for binding events in real time [7]. Several data processing methods have targeted SNR improvement of propagating SPR sensors: the centroid and full-width-at-half-maximum tracking method [8,9], principle component and locally weighted parametric regression [10], optimal linear data analysis [11], polynomial curve-fitting of the measured curve [12], statistical hypothesis testing [13], and a double projection method [14]. The integrated response method was applied to nanohole-structures [15], which is based on the extraordinary transmission of light arising from the propagating surface plasmon resonance [16–19]. The normalized-difference integrated-response method was used to improve the sensitivity of multispectral thin film biosensing imaged with 3-D photonic crystals [20]. However, less effort has been previously made towards signal processing methods to improve the SNR for LSPR sensors.

Here we present a simple projection method based on a one-dimensional reference matrix: this requires significantly simpler instrumentation compared to the previously described spectro-angular double projection method and yet results in a significant improvement in performance [14]. The results and discussion section presents performance details and comparison to the established methods.

## 2. Projection method

The double projection method, on which the proposed method is based, was introduced to improve the signal to noise ratio of a spectro-angular SPR sensor [14]. Its principle of operation is briefly explained here; Spectro-angular reflectance maps for a set of different refractive indices were numerically calculated in advance. Singular value decomposition was then used to extract a basis set from these 2-D images. Two projections were performed against the basis set: i) the normalized simulated images were projected against the basis matrix yielding a weight matrix; and the measured spectro-angular images (arising from samples with unknown refractive indices) were projected against the basis set to form a set of weight vectors. The weight vectors were then projected against the simulated weight matrix yielding a solution vector (the name of the method was given based on the second projection process). The solution vector was then interpolated to improve precision of refractive index estimate. The method achieved a 3-order of improvement in signal to noise ratio (in numerical simulation) [14]. However, the experimental complexity of the spectro-angular interrogation SPR system may be an issue if a simple platform is desired.

The single projection method, proposed here, simplifies the double projection method by projecting the normalized measured data (normalized vectors) onto a simulated reference set and interpolating the solution vector to estimate unknown refractive indices of the measurands. The remainder of this section provides more details about the new approach.

The finite difference time domain was used to calculate the transmission spectra of the nanotube structures: we used OptiFDTD commercial software [21] to model the nanostructures and optimize their dimensions to match the performance of the fabricated structures. The simulation was then repeated to obtain a set of transmission spectra spanning the refractive index ( $RI$ ) range ( $n_{min} - n_{max}$ ) with  $1 \times 10^{-3}$  resolution. The simulation vectors representing the simulated spectra were normalized by dividing each transmission vector ( $T$ ) by its norm, and concatenating them to build the reference matrix ( $M$ ) as follows

$$T_n = \frac{T}{||T||} \quad (1)$$

$$M = \begin{bmatrix} T_{n11} & T_{n12} & \dots & T_{n1j} \\ T_{n21} & \ddots & \ddots & T_{n2j} \\ \vdots & \ddots & \ddots & \vdots \\ T_{ni1} & T_{ni2} & \dots & T_{nij} \end{bmatrix} \quad (2)$$

where the rows ( $i$ ) span the  $RI$  range of interest, and the columns ( $j$ ) correspond to the wavelength data points (We used 750 data points, and 0.2 nm wavelength resolution) as illustrated in Fig. 1.

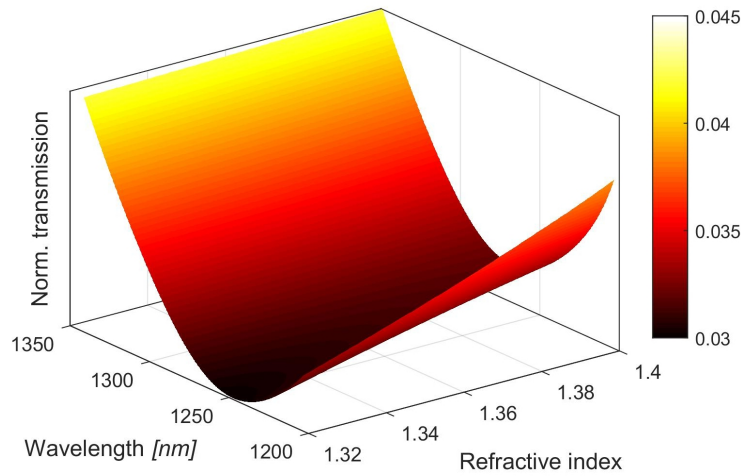


Fig. 1. A 3-D representation of the projection reference matrix (obtained from the FDTD simulation) for a set of refractive indices spanning the  $RI$  range (1.318–1.4), Simulation used 750 wavelength data points (0.2 nm resolution).

To estimate the refractive index of an unknown sample, the measured transmission spectrum from the sample is represented by a vector ( $v$ ) that is divided by its norm to reduce the effect of intensity fluctuations.

$$v_n = \frac{v}{||v||} \quad (3)$$

Now the normalized vector ( $v_n$ ) for the unknown  $RI$  is projected onto the reference matrix ( $M$ ) vector by vector to obtain the solution row vector ( $S$ ) whose elements provide the degree of similarity between the measured and the simulated spectra.

$$S = M \cdot v_n \quad (4)$$

The solution row vector ( $S$ ) can be interpolated over the  $RI$  range. This approach is illustrated in Fig. 2: Fig. 2(a) shows two noisy measured transmission curves corresponding to two different bulk refractive indices. Fig. 2(b) shows the solution row vectors calculated for each. Interpolating the curve improves the precision of the method, and the abscissa of the maximum provides the  $RI$  estimate. Therefore, the noisy measured transmission curve (providing the resonance shift) was transformed into a smooth curve, extracting the refractive index of unknown solutions directly.

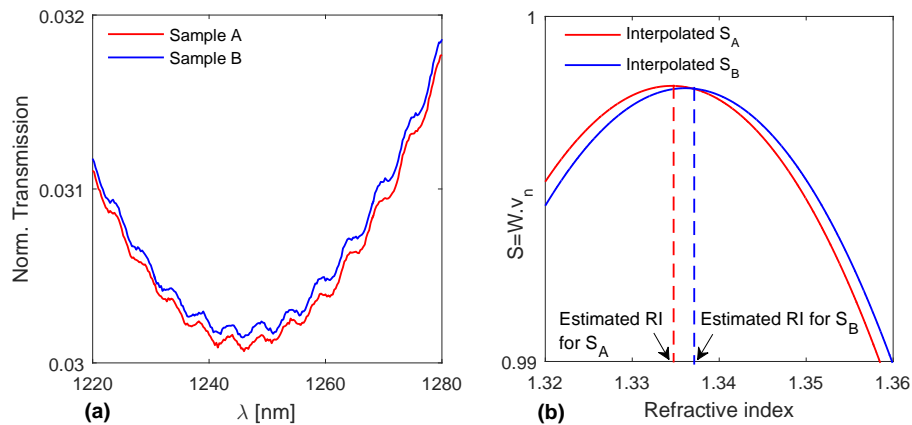


Fig. 2. (a) Normalized transmission vectors for unknown samples (A and B): the curves are affected by noise and high frequency interferences (ripples) that complicates tracking the transmission dip reducing the sensor accuracy. (b): Interpolated curves for the solution row vectors for unknown samples (A and B) revealing estimated refractive indices of 1.3346 and 1.3361, respectively: the entire measured curve in (a) was used here instead of using a single resonance wavelength as in the dip-finding method.

### 3. Methods

#### 3.1. Simulation of nanotube structures

Commercial OptiFDTD design tool [21] was used to simulate periodic nanotube structures and optimize them to have their transmission curve match the measured counterpart. A single structure unit of hexagonal lattice is used in the simulation, and periodic boundary conditions were forced to simulate the infinite number of nanotubes. The Drude Lorentz model was used for the gold material properties, and a value of 1.53 refractive index was used for the COP substrate. A Gaussian-modulated continuous wave was used to excite the nanostructures with a normal incidence. Numerical optimization has been performed to the simulated structure to match the simulated spectra with the measured counterparts. The simulation was repeated for the entire refractive index range. The sensitivity of the sensor can be calculated as the slope of the resonance shift with respect to the refractive index change, the calculated sensitivity was 582.9 nm/RIU.

#### 3.2. Fabrication of the nanostructures and fluidic channel

Nanoimprint lithography technique was used to fabricate the nanotube structures. The fabrication procedure is described in detail elsewhere [5]. Briefly a silicon mold (the nanotube stamp) is pressed into a heated cyclic olefin polymer (COP), and then released to form nanopillars; the structures are coated with gold, and the top layer of gold is removed by reactive ion etching, yielding gold nanotubes. Fig. 5 shows a scanning electron microscopy (SEM) image of the fabricated structures that are uniformly distributed on the COP substrate.

The fluidic channel was fabricated by using Polydimethylsiloxane (PDMS) replica molding method: UV photolithography is used to pattern SU-8 negative resist on a silicon wafer, then immersed in the SU-8 developer, blown dry with Nitrogen gun, and postbaked to form the stamp that can be used to replicate the channels on PDMS as presented in [22]. The grooved part of the PDMS can be bonded to the sensing chip and the fluids can be injected through the in/outlets as shown in Fig. 5(a).

### 3.3. Sensor functionalization and samples preparation

The functionalization process included the preparation (cleaning) of the sensing chip, incubation, and post-cleaning of the chip before any sensing experiments: the sensing surface was cleaned by isopropyl alcohol and deionized (DI) water, then plasma treated to remove any organic objects. The sensing chip was then incubated, for biotin labeling, in 10 mM phosphate buffer solution (pH 7.2) of 200  $\mu\text{M}$  of Formula-(6-[biotinamido]hexyl)-3'-(2'-pyridyldithio)propionamide. The streptavidin solutions were prepared by dissolving streptavidin powder in a 50 mM Tris buffer (pH 8) [3].

## 4. Results and discussion

This section presents comparative results based on simulated results and bulk and surface binding sensing results.

### 4.1. Comparison to established methods

This section compares the projection method to previously published signal processing methods based on simulated results. We used the FDTD simulation to obtain transmission curves, corresponding to known changes in bulk RI. In order to determine the accuracy of the methods, we applied each method to the simulated data to estimate the RI change used in the simulation. To investigate the effect of noise on the accuracy of each method, we introduced a Gaussian noise to the simulated transmission curves, and used each signal processing method in estimating the RI change.

First, we determine the accuracy of the projection method with respect to the RI interval in the reference matrix as shown in Fig. 3(a), the medium RI is changed by  $1 \times 10^{-5}$  and  $5 \times 10^{-5}$  in the simulation, and the corresponding transmission curves were projected against reference matrices of different RI step size. An accuracy of  $10^{-7}$  RIU can be obtained using a reference matrix with a  $1 \times 10^{-4}$  RI step size. We also introduced a Gaussian noise to the simulated transmission curves to investigate the stability of the method with respect to noise levels, as shown in Fig. 3(b), the error in the estimated RI change based on a noisy transmission curve can be as low as 0.2%.

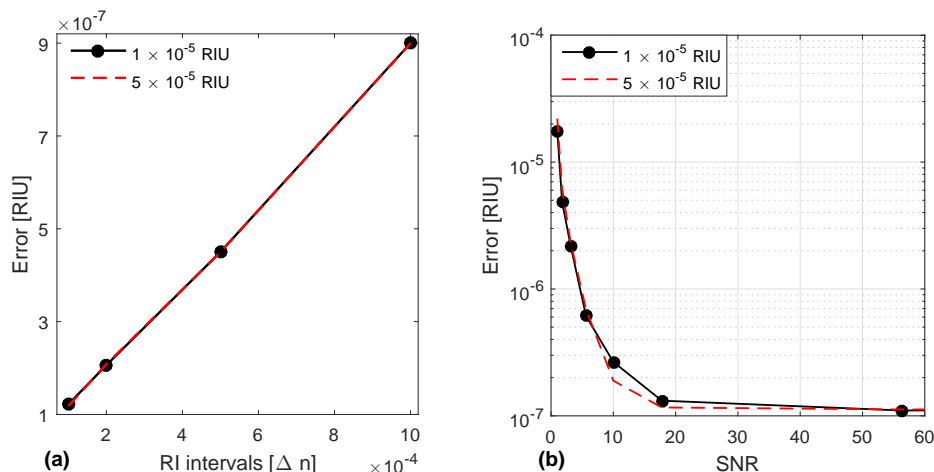


Fig. 3. (a) Calculated error in the estimated RI change with respect to the RI interval in the reference set, (b) error in estimated RI change, calculated as the difference between the estimated RI changes and the ideal values ( $1 \times 10^{-5}$  and  $5 \times 10^{-5}$ ).

Now we apply all the methods to the same simulated noisy data in order to estimate the RI change, the reference set is used to obtain a calibration curve for each method, and the slope of



each curve provides the sensitivity factor used in determining the RI change (known in this case to test the accuracy of each method). The dynamic-baseline centroid method [9] uses a threshold value (usually the FWHM) to estimate the resonance wavelength ( $\lambda_r$ ) as follows

$$\lambda_r = \frac{\sum_j j (R_{thresh} - R_j)}{\sum_j (R_{thresh} - R_j)} \quad (5)$$

where  $R_j$  are the transmission values below the threshold value ( $R_{thresh}$ ), and (j) correspond to the wavelength data points. The fixed boundary method uses the same wavelength range over which the centroid calculations— for all the measured spectra—are performed. This simplifies the calculations as follows

$$\lambda_r = \frac{\sum_j j R_j}{\sum_j (R_j)} \quad (6)$$

where  $R_j$  spans the response (transmission) values over the wavelength range. The integrated response method was introduced in order to improve the performance of a nanohole SPR sensor and has previously been compared to the peak shift method (dip-finding method) and normalized difference integrated response [15]. The integrated response method is based on intensity difference calculations using the following equation [15]

$$I_{int} = \left( \int_{\lambda_1}^{\lambda_2} |D^2(\lambda) - \overline{D^2(\lambda)}| d\lambda \right)^{1/2} \quad (7)$$

where  $D(\lambda) = R_{ref}(\lambda) - R(\lambda)$  is the difference between the reference and measured signals, and  $\overline{D^2(\lambda)}$  is the mean of the total squared differences. The normalized difference integrated response (NDIR) technique uses data within a wavelength range ( $\lambda_1 - \lambda_2$ ) by applying the following equation [20]

$$NDIR = \int_{\lambda_1}^{\lambda_2} \left| \frac{R_{ref}(\lambda) - R(\lambda)}{R_{ref}(\lambda)} \right| d\lambda \quad (8)$$

where  $R_{ref}(\lambda)$  and  $R(\lambda)$  are the reference and measured signals respectively.

After applying these methods on the simulated data to determine a RI shift of  $5 \times 10^{-5}$ , a Gaussian noise was added to the extinction curves and the effect was also investigated. As shown in Fig. 4, the projection method outperforms the established methods as the error is in the range of  $1 \times 10^{-7}$  that is one order of magnitude improvement to the dynamic-baseline centroid and NDIR methods, and two orders of magnitude improvement to the integrated response and fixed-boundary centroid methods, and three orders of magnitude improvement to the conventional dip-finding method.

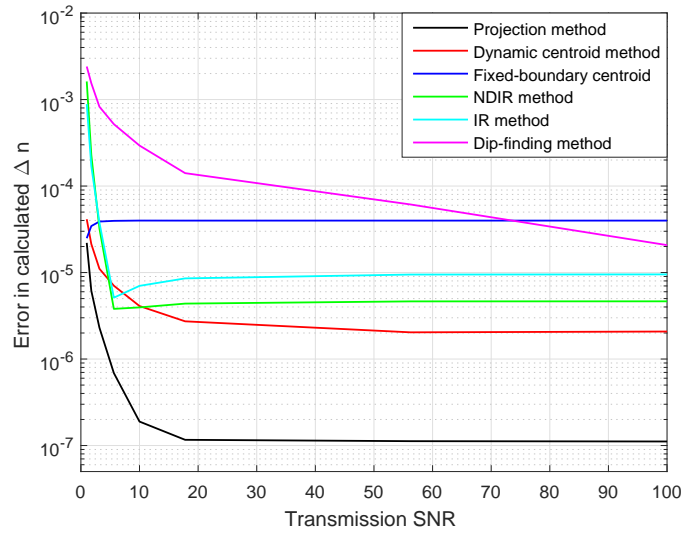


Fig. 4. Calculated error with respect to the noise level added to the simulated transmission curves, the projection method is superior to the other methods in terms of accuracy ( $1 \times 10^{-7}$  RIU error) and stability against noise as the error is as low as  $5 \times 10^{-6}$  (10% error) even with noisy transmission curves (SNR  $\approx 3$ ).

#### 4.2. Bulk RI and surface binding sensing results

This section presents sensing results based on the projection method and provides a comparison to the published methods in terms of SNR improvement and computational complexity. Fig. 5(a) shows the experimental set-up and the sensing chip.

Multiple transmission spectra were obtained for ethanol solutions of different concentrations. The measured sensitivity,  $S$ , and the figure of merit, FoM, for the nanostructures are  $\sim 582.9$  nm/RIU, and 1.2 /RIU, respectively. The FoM was calculated as  $\text{FoM} = S/\text{FWHM}$ , where FWHM is the full width at half maximum of the measured transmission curve. The low figure of merit resulted in a significant uncertainty in determining the location of the resonance minimum when the dip finding method was used, as shown in Fig. 6 (left Y-axis). The projection method improved the results as the entire measured spectra were transformed into normalized vectors and projected on the reference matrix (shown in Fig. 1) by using Eq. (3) and Eq. (4). This also provided a direct measurement to the refractive index of the ethanol solutions as shown in Fig. 6 (right Y-axis).

To provide a fair and complete comparison, the measured resonance wavelengths obtained by the dip-finding method are translated into refractive indices by using the FDTD calculated sensitivity ( $S_B = 582.9$  nm/RIU) as follows

$$n = n_0 + \frac{\Delta\lambda_r}{S_B}, \quad \Delta\lambda_r = \lambda_r - \lambda_0 \quad (9)$$

where  $n$  is the calculated refractive index based on the measured resonance wavelength,  $\lambda_r$ ;  $n_0$  is the buffer refractive index; and  $\lambda_0$  is the resonance wavelength when buffer solution is injected.

To validate the results of the FDTD sensitivity calculations and the projection method, we had to compare the experimentally determined refractive indices with reported values in the literature. However, the reported values for ethanol-water mixture are at 589.29 nm [23], whereas the values determined here are at 1247 nm. We used the improved Cauchy formula [24] to estimate the



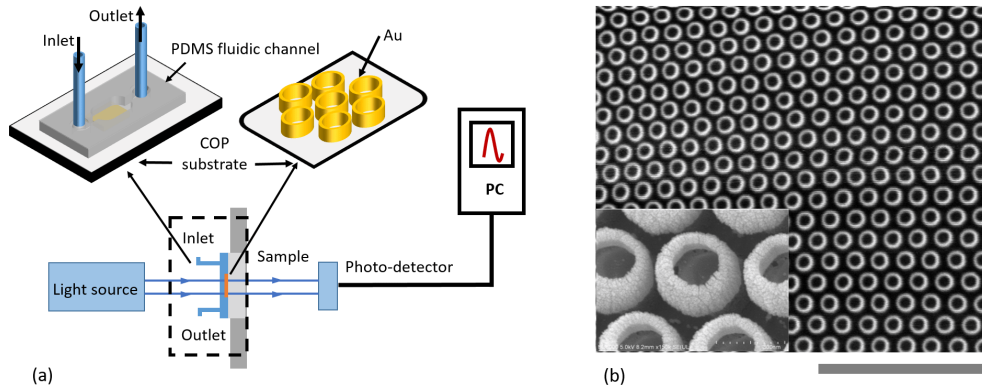


Fig. 5. (a): Experimental sensing set-up: Cary 5000 spectrometer was used in the sensing experiment, a baseline with PDMS channel and buffer solution is taken first, then the measurements were performed on the functionalized nanotube structures, the solutions were injected using an automatic pump (Harvard Apparatus-PicoPlus) with 200  $\mu\text{L}/\text{min}$  flow speed. The inset shows the PDMS fluidic channel: the grooved part is bonded to the surface of the COP (sandwiching the nanostructures between the PDMS and COP, the inlet/outlet are punched using a biopsy puncher to insert the fluidic tubes). (b): SEM image of the fabricated structures: inner diameter= 200 nm, gold layer thickness= 60 nm, and pitch= 400 nm. The gray scale measures 3  $\mu\text{m}$  and 400 nm with respect to the outer image and the inset, respectively.

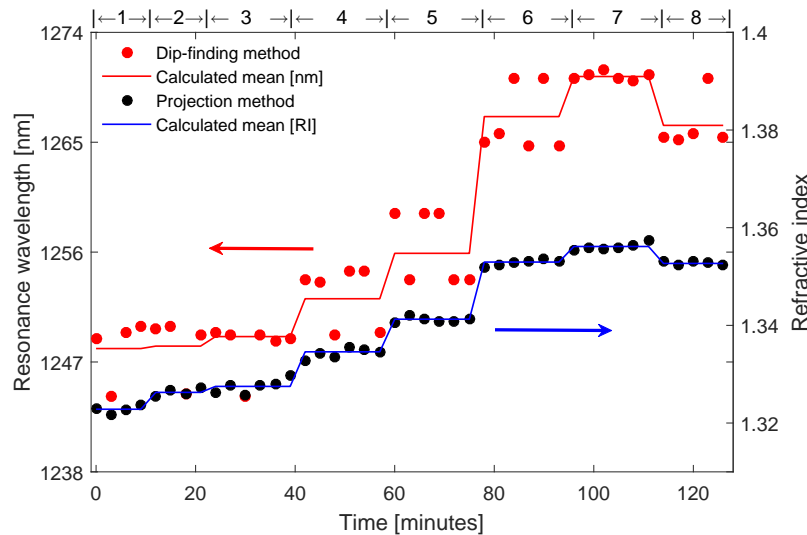


Fig. 6. Real time sensing measurements for ethanol solutions with different concentrations ([1]: 0%, [2]: 2%, [3]: 4%, [4]: 16%, [5]: 30%, [6]: 50%, [7]: 80%, [8]: 100%) in the case of: dip-finding method (left Y-axis); and projection method (right Y-axis) where the refractive index is directly extracted.

correct index values at the sensor's resonance wavelength (1247 nm)

$$n^2(\lambda) = C_0 + \frac{C_1}{\lambda^2} + \frac{C_2}{\lambda^4} + C_3\lambda^2 \quad (10)$$

The Cauchy parameters for DI water and ethanol are known, which is not the case for the ethanol-DI water mixture. This motivated us to estimate the Cauchy parameters for all the tested ethanol solutions (0% – 100%). Since the refractive indices for the 50% and 100% ethanol solutions are approximately equal, we can use the known Cauchy parameters for pure DI water and ethanol (0%, 50%, and 100%) in curve fitting each Cauchy parameter for the mixtures and write these parameters in terms of fitting coefficients of the form

$$C_n = p_0 + p_1w + p_3w^2 \quad (11)$$

where the subscript ( $n = 0, 1, 2, 3$ ) denotes the order of the Cauchy parameters, ( $w$ ) is the concentration of ethanol in percent weight, and ( $p_0, p_1, p_3$ ) are the fitting coefficients. Therefore, we obtained four equations to calculate the four Cauchy parameters for all ethanol solutions (of different concentrations) as shown in table 1.

Table 1. Fitted Cauchy parameters for all the tested ethanol solutions at 20 °C

%w	$C_0$ $\times 10^{-3}$	$C_1$ $\times 10^{-3}$	$C_2$ $\times 10^{-3}$	$C_3$ $\times 10^{-3}$
0	1768.80±1.34	2.37±0.93	0.87±0.17	-16.51±0.48
2	1772.630 ±1.378	2.619±0.96	0.84±0.175	-15.74±0.49
4	1776.350 ±1.416	2.85±0.98	0.80±0.179	-14.99±0.51
16	1796.53±1.62	4.13±1.12	0.63±0.204	-10.94±0.58
30	1815.360±1.8	5.33±1.25	0.47±0.227	-7.16±0.65
50	1833.47±1.99	6.48±1.38	0.31±0.25	-3.52±0.71
80	1841.23±2.07	6.97±1.43	0.24±0.26	-1.96±0.74
100	1833.47±1.99	6.48±1.38	0.31±0.25	-3.52±0.71

To validate the fitted Cauchy parameters, we used them along with the Cauchy formula [Eq. (10)] to calculate refractive index of ethanol solutions at 589.29 nm, and the results agree well with those reported in [23], as shown in Fig. 7(a).

For ethanol-DI-water mixture, the peak refractive index occurs at 80 – 82%; the peak location is insensitive to wavelength as it occurred at 77% ethanol solution measured at different wavelengths ~589 nm, 1310 nm and 1550 nm, at 25 °C [25]. The drop in refractive index (for concentrations higher than the peak location) is attributed to the ethanol water dissociation and molecular repulsive forces: a close packing of water ethanol increases with concentration and reaches its maximum at 82% where the mixture volume reaches the minimum. As the concentration of ethanol exceeds 82%, the repulsive forces between water and ethanol molecules increase the intermolecular spaces, and the RI decreases as a result [26]. The peak location is slightly influenced by the temperature: it occurs with 82.86% ethanol solution at 20 °C ; with 77.35% ethanol solution at 30 °C; and with 82.86% ethanol solution at 35 °C [26]. The refractive indices reach their maximum values at 20 °C; this effect has been taken into account in fitting the Cauchy parameters as we based the calculations on the Cauchy parameters for DI-water and ethanol at 20 °C.

Now, we can use the fitted Cauchy parameters and the Cauchy formula to calculate the refractive indices of the ethanol solutions at the sensor operating wavelength (1249 nm), and compare them with the measured sensing results. Fig. 7(b) shows the measured results agree well with the calculated counterparts with the exception of a discrepancy at around the 30% concentration.

Now we compare the projection method with the methods discussed in earlier sections, we translate the response of each method to a refractive index value using Eq. (9); however, each method provides a different value as a response (centroid methods estimate the resonance locations and the NDIR and integrated response methods provide normalized intensity based

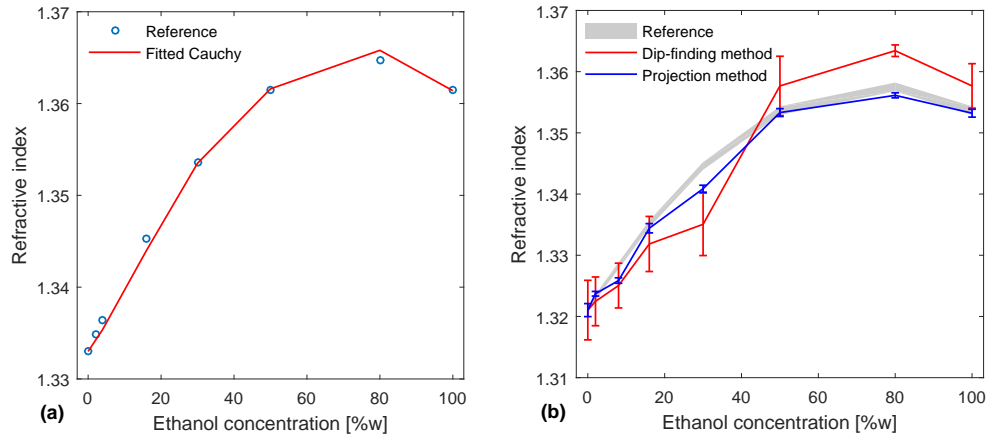


Fig. 7. (a): Calculated refractive index based on the fitted Cauchy parameters in table 1, and the improved Cauchy formula [Eq. (10)] at 20 °C and 589.29 nm wavelength: the estimated values agree well with those of reference [23].(b): Sensor response to bulk concentrations using the projection and dip-finding methods: the error bars correspond to repeated measurements (at 20 °C, and 1247 nm resonance wavelength), the reference curve was obtained using the Cauchy empirical formula, Eq. (10), and the fitted Cauchy parameters in table 1 — calculated using the polynomial curve fitting — at the same temperature and sensor operating wavelength (20 °C and 1247 nm).

responses). The centroid methods reveal different resonance locations due to the asymmetrical shape of the resonance curves. Therefore, the sensitivity has to be recalculated according to the response of each method, the calculated values for the sensitivity are as follows: 525.74 nm/RIU for the fixed-boundary centroid method; 577.9 nm/RIU for the dynamic-baseline centroid method; 0.401/RIU for the integrated response method; and 5478.4 /RIU for the NDIR method. The RI change can be estimated as the ratio of the response of each method to its sensitivity,  $\Delta n = \Delta R / S_B$ , where  $\Delta R$  denotes the response change with respect to the ethanol concentrations ( $\Delta \lambda$  in the case of the centroid methods, and  $\Delta I_{int}$ , or  $\Delta NDIR$  in the case of integrated response and NDIR methods). Fig. 8 compares the projection method with the reference methods. Signal to noise ratio is calculated based on the mean (signal) and standard deviation (noise) of the measured data at each step (representing the change in ethanol concentration in the bulk solution) as follows

$$SNR(dB) = 10 \times \log\left(\frac{\overline{\Delta n}}{\sigma}\right) \quad (12)$$

where  $\overline{\Delta n}$  and  $(\sigma)$  are the steady state mean and standard deviation (representing noise) of the refractive index shift. The sensor refractive index resolution can be estimated as  $\Delta n \sim 3 \sigma$ , corresponding to  $SNR \sim 3 (\approx 4.8 \text{ dB})$ . The error was calculated as the average of the percentage error in the measured RI changes over the entire range of ethanol concentrations

$$\varepsilon = \frac{1}{m} \sum_{i=1}^m \frac{|\Delta n_i - \Delta n_{true,i}|}{\Delta n_{true,i}}$$

where  $\Delta n_i$  are the measured RI changes, and  $\Delta n_{true,i}$  are the true values for the RI changes corresponding to the ethanol concentrations. Table 2 provides a complete list of the calculated values of SNR, RI resolution and error in RI change. The projection method outperforms the dip-finding method, the fixed-boundary centroid method, the integrated response method and

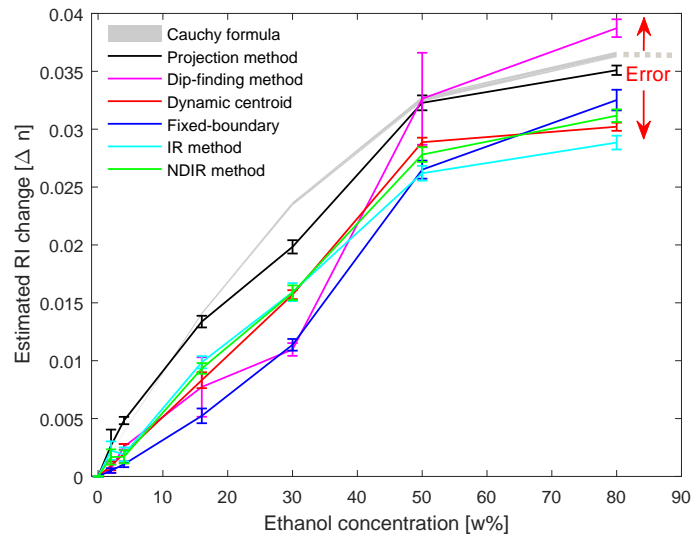


Fig. 8. RI change measured by the projection method for ethanol solutions of different concentrations. The RI change estimated by the reference methods are also shown: the measured response of each method in Fig. 6 was used to calculate the RI change using Eq. (9) for a better comparison with the projection method. The standard deviation of the measured refractive indices are represented by error bars for each method, and by the line width for those based on the Cauchy formula.

the NDIR method in terms of SNR improvement, and it provides essentially the same SNR performance as the dynamic-baseline centroid method. The projection method provides a more accurate estimation of the refractive index changes based on simulated and measured results. Based on the FDTD results [Fig. 4], the error was about 0.2% and 10% for the projection and dynamic-baseline centroid methods respectively; and based on the measured data, the error was  $\sim 14\%$  and  $\sim 33.97\%$  for the projection and the dynamic-baseline centroid method, respectively. The projection method also provides the lowest RI resolution along with the NDIR method. The high error values revealed by the fast centroid method are attributed to the wide boundaries (wavelength range) that were used in the calculations. A narrower boundary would decrease the sensor RI dynamic range as an upper limit of refractive index has been previously reported to be 1.35 RIU [27]. Providing a direct measurement for the refractive index is considered as another advantage of the projection method.

Temperature fluctuations and spectral resolution also have significant effects on the sensor performance; the spectral resolution of the spectrometer used in our experiments was (0.2 nm); this limited the refractive index resolution to  $\sim 7.5 \times 10^{-4}$  RIU. However, this is close to the value that was reported for a high resolution LSPR sensor  $\sim 3 \times 10^{-4}$  RIU [28]. In a recent work, a LSPR sensor, based on metallic nanostructures, achieved a FOM  $\sim 108$  (narrow FWHM  $\sim 9.5$  nm, and high RI sensitivity  $\sim 1,015$  nm/RIU) [29]. Although this FOM is much higher than that of the nanotube structures, the resolution was only  $\sim 2 \times 10^{-4}$  RIU due to the limited spectral resolution of the spectrometer  $\sim 0.1$  nm, and the measured signal was constrained to a specific angle to excite the mode of the nanostructures [29]. The proposed projection method achieved the same RI resolution although the measured curves were extremely broad and noisy. Moreover, the spectra were generated by a direct transmission measurement set-up.

We also conducted surface binding experiments to determine the performance of the projection

Table 2. Comparison between the projection method and the published counterparts.

<i>Method</i>	SNR [dB]	RI resolution [RIU]	Error in estimated $\Delta n$
Proposed Projection method	32.07	$7.5 \times 10^{-4}$	14.62%
Dip-finding method [7]	8.95	$1 \times 10^{-2}$	33.94%
Dynamic-baseline centroid [9]	32.97	$1.95 \times 10^{-3}$	33.97%
Fixed-boundary centroid [27]	24.34	$1.35 \times 10^{-3}$	48.46%
Integrated response [15]	21.47	$7.5 \times 10^{-4}$	27.92%
NDIR method [20]	24.22	$4 \times 10^{-4}$	27.58%

method in estimating the effective refractive index change due to surface binding. We adopted the functionalization protocol used in [3] for biotin functionalization and prepared the streptavidin solution (as explained in section 3.3). Fig. 9 (a,b) shows the sensogram based on the projection method and its counterparts. Since the bulk RI resolution was improved by one order of magnitude compared to the dip-finding method, the projection method can improve the sensor limit of detection (LoD) by a factor of  $\sim 10$ . The LoD can be measured as the minimum detectable streptavidin concentration change, corresponding to the minimum measured RI change (RI resolution). As observed in Fig. 9 (c), the least LoD was achieved by the NDIR method, followed by the proposed projection method and the integrated response method, the fixed-boundary centroid method, and the dynamic-baseline centroid method. The dip-finding method revealed the highest LoD, and a change of  $200 \mu\text{g/mL}$  of streptavidin was undetectable by this method [steps: 2 and 3, Fig. 9 (a, b)]. However, the sensor LoD depends on the analyte to be detected, its molecular weight, and the binding conditions during the experiment. Therefore, we have used the bulk RI resolution to compare the projection method with the previously published approaches. Although the NDIR method provided an improved response here, but it has previously reported that the method incurred a response instability and showed a distorted real time sensogram based on a surface binding experiment [15].

It is also important to consider computational complexity; the reference methods described above have a computational complexity that grows as  $\sim O(N)$  where  $N$  is the number of wavelength samples. During operation, the proposed projection method projects the measured spectrum against a set of pre-calculated spectra, indicating a computational complexity of  $\sim O(pN)$  where  $p$  is the number of reference spectra (typically 40). As a result, it does require more computation than the other methods, but given the power of even modest current microprocessors, this does not impact the ability to use it for real-time measurement (as shown in our measurement of binding kinetics).

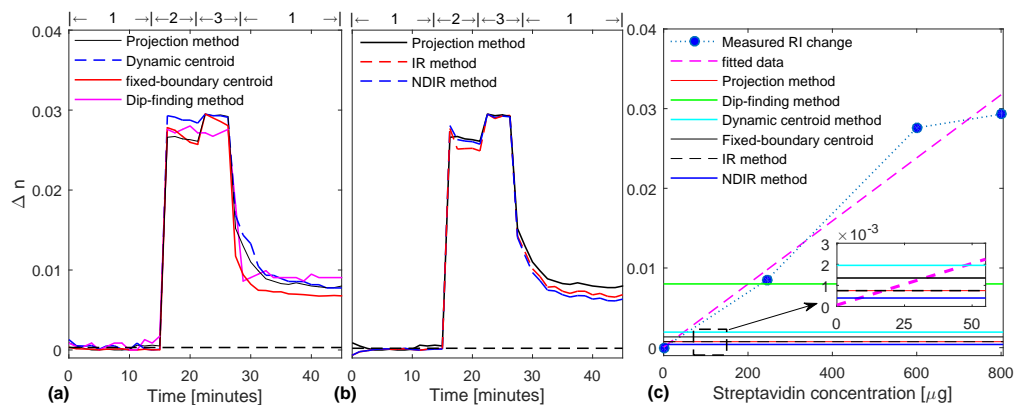


Fig. 9. (a), (b) Sensor response to biotin-streptavidin surface binding events, calculated using the projection method and the published counterparts. The scale over the figure denotes the sequence of flushing the solutions as [1]: Tris buffer solution was injected for the first 15 minutes to create a baseline, then streptavidin solutions – with [2]: 0.6 mg/mL and [3]: 0.8 mg/mL concentrations – were injected simultaneously. Tris buffer silane was injected as a final step to flush unbound streptavidin. (c) RI change due to the change in streptavidin concentrations. The horizontal lines, corresponding to the RI resolution achieved by each method, intersect the RI curve at the minimum detectable streptavidin concentration (LoD)

## 5. Conclusion

In summary, we have introduced a new signal processing technique to improve signal to noise ratio of localized surface plasmon resonance biosensors. The method provided the refractive index directly from extremely broad and noisy transmission spectra. The measured refractive indices agree well with those calculated using the fitted Cauchy parameters with a slight discrepancy at 30% concentration. The projection method improved the SNR by one order of magnitude ( $\sim$  ten-fold increase compared to the absolute SNR with the dip-finding method), and hence decreased the RI resolution from  $1 \times 10^{-2}$  RIU in the case of dip-finding method to  $7.5 \times 10^{-4}$  RIU. The projection method provided a comparable SNR relative to the dynamic-baseline centroid method; however, it outperforms the dynamic-baseline centroid method in terms of accuracy, based on both simulated and measured results. The projection method provides a higher SNR compared to the integration technique and normalized difference integrated response methods, although the latter provided the same RI resolution. The projection method avoids some of the previously reported limitations of the reference methods, such as the introduction of distortions to the sensogram (reported for the NDIR method [15]) or reductions in dynamic range (reported for the fixed-boundary centroid method [27]). The projection method does however require a modest increase in computation. Although the measured RI resolution achieved by the proposed projection method is  $7.5 \times 10^{-4}$  RIU, the simulated results reveal that the method can resolve a RI change of  $\sim 1 \times 10^{-5}$  RIU. This limit is due to the spectral resolution of the spectrometer (0.2 nm). The results can be improved by using a temperature controller and a photodiode array detector with improved resolution.

## Acknowledgments

We thank Sandrine Filion Côté and Minh Tran for discussing the projection method, and Ayo Olanrewaju for the help with the PDMS replica moulding method. We thank Professor Bruce Lennox and Professor David Juncker for providing access to the spectroscopy and fabrication facilities. The OptiFDTD design tool was provided by CMC Microsystems.